Nonlinear Aspects of the Climate Response to Greenhouse Gas and Aerosol Forcing

JOHANN FEICHTER AND ERICH ROECKNER

Max Planck Institute for Meteorology, Hamburg, Germany

ULRIKE LOHMANN

Dalhousie University, Halifax, Nova Scotia, Canada

BEATE LIEPERT

Lamont-Doherty Earth Observatory, Columbia University, Palisades, New York

(Manuscript received 25 June 2003, in final form 8 October 2003)

ABSTRACT

In a series of equilibrium experiments the climate response to present-day radiative forcings of anthropogenic greenhouse gases and aerosol particles is calculated. The study was performed with a model system consisting of the ECHAM4 atmospheric general circulation model coupled to a slab ocean and thermodynamic sea ice model. The model includes transport of the relevant chemical constituents, a sulfur chemistry model that calculates sulfate production in the gas and aqueous phase, and an aerosol model that accounts for source and sink processes. The aerosol cycle, the hydrological cycle, and the atmospheric dynamics are fully interactive. The climate response to aerosol forcing is not just a mirror image of the response to greenhouse forcing. This applies to the temperature changes, which are regionally more uniform for greenhouse forcing than for aerosol forcing as is already well known, and, in particular, to the hydrological cycle: the global hydrological sensitivity (Δprecip/Δtemp) to a 1-K surface temperature change is almost 3 times higher for aerosol forcing than for greenhouse forcing. When both forcings are combined, a global warming is simulated while evaporation and precipitation decrease by about 2% K^{-1}, resulting in a negative hydrological sensitivity. A strong dependency of the response to the type of forcing has also been found for the cloud water content and, consequently, for the change in cloud radiative forcing, which is substantially larger in the combined forcing experiment than in either of the individual forcing experiments. Consequently, the global warming for combined forcing is significantly smaller (0.57 K) than that obtained by adding the individual changes (0.85 K). Due to feedbacks between temperature changes and the hydrological cycle the simulated aerosol load, applying the same source strength, is considerably lower in a warmer climate (-17% K^{-1} warming). A consequence of this aerosol–temperature feedback could be that a future increase in greenhouse gases may reduce the aerosol burden even if the source strength would not change.

1. Introduction

Anthropogenic emissions from fossil fuel combustion and biomass burning have considerably modified the chemical composition of the atmosphere. The response of the climate system to the increases of infrared-active gases—the anthropogenic greenhouse effect—has been the subject of intense research since the 1970s. In contrast, the climate response to increasing aerosol particles, has only started to receive significant attention during the last decade because of the complexity of the problem. Unlike most greenhouse gases, which are long lived and therefore well mixed in the troposphere, aerosols have a short atmospheric residence time resulting in substantial spatial and temporal variability. Estimates of the aerosol climate impact are further complicated by the fact that the forcing depends not only on the aerosol mass distribution but additionally on intensive properties like particle number concentration, size distribution, and state of mixture. Aerosol particles influence the climate system by scattering and absorbing solar radiation and to a lesser extent by absorbing and emitting thermal radiation. In addition to these so-called direct effects, aerosols modify the microphysical properties of clouds by acting as cloud condensation nuclei (CCN) or ice nuclei (IN), called the first indirect effect. The ''semidirect effect'' (Hansen et al. 1997), the ''lifetime'' or ''second indirect effect'' (Albrecht 1989), or the ''glaciation indirect effect'' (Lohmann 2002) are essentially responses of the climate system to these mechanisms. Apart from the semidirect effect, which reduces cloudiness and enhances solar surface insolation, all oth-

Corresponding author address: Dr. Johann Feichter, Max Planck Institute for Meteorology, Bundesstr. 55, Hamburg 20146, Germany. E-mail: feichter@dkrz.de

er effects contribute to a reduction in solar radiation at the earth's surface with consequences for its heat budget including changes in thermal emission, sensible and latent heat fluxes, and subsequent changes in water vapor transport, cloud formation, precipitation, and evaporation (Roeckner et al. 1999; Ramanathan et al. 2001). Aerosol cooling of the atmosphere reduces the water vapor holding capacity of the atmosphere. In contrast, an increase in aerosol particles may enhance the liquid water content of clouds and the cloud optical thickness as a result of suppressed rain formation.

The first estimates of the direct aerosol effect were performed with radiation convection models (Charlson and Pilat 1969; Rasool and Schneider 1971; Chylek and Coakley 1974). Starting in the 1990s, global chemistry transport models have been used to calculate global aerosol distributions and to estimate the aerosol radiative forcing. Langner and Rodhe (1991) pioneered the prediction of the mass of sulfate particles. Since this work, progress has been made in taking more aerosol species into account and in refining the aerosol physical approaches (e.g., Kiehl and Briegleb 1993; Feichter et al. 1997; Lohmann et al. 1999; Rasch et al. 2000a). Based on findings during the Tropospheric Aerosol Radiative Forcing Observational Experiment (TARFOX; Hobbs 1999) and the Indian Ocean Experiment (INDOEX; Ramanathan et al. 2002) measurement campaigns the role of absorbing aerosols in the climate system found more attention in the scientific discussion. Model studies guided by observations during INDOEX (Ackerman et al. 2000) and global climate model studies (Lohmann and Feichter 2001; Jacobson 2001) confirmed the cloud-dissolving or semidirect effect of absorbing aerosols first proposed by Grassl (1979).

There is a strong coupling between aerosols, clouds, and precipitation processes. For example, aerosol-induced changes of the hydrological cycle feed back on the aerosol distribution. Hence, for estimating the climate effect of anthropogenic aerosols, global climate models are required to have a fully interactive treatment of different size resolved aerosol species. As shown in numerous studies with climate models (Mitchell 1987; Dai et al. 1997; Timmermann et al. 1999; Roeckner et al. 1999; Douville et al. 2002; Allen and Ingram 2002), increasing levels of greenhouse gases affect the hydrological cycle as well. On a global scale, greenhouse warming increases evaporation, precipitation, and tropospheric water vapor. Moreover, cloud water content and cloud optical thickness are generally enhanced (e.g., Roeckner et al. 1999). These findings are confirmed by observations and model simulations by Tselioudis et al. (1998) in the midlatitudes. However, at low latitudes, they found a decrease of cloud optical thickness with increasing temperature, in both simulations and observations. This anticorrelation occurred despite increases in cloud geometrical depth because of enhanced precipitation formation that decreased the cloud liquid water content.

In this paper we investigate the following questions: (i) What is the climate response to increases in atmospheric greenhouse gas concentrations and aerosols emissions during the past century, (ii) can the combined effect of greenhouse gases and aerosols be estimated by simply adding the individual contributions, and (iii) is the atmospheric aerosol load dependent on the climate state, that is, are aerosol–climate feedbacks relevant? We address these questions by using an atmospheric general circulation model, including the aerosol effects mentioned above, coupled to a slab ocean model. Three pairs of climate equilibrium experiments were performed. Each pair consists of a control experiment with preindustrial conditions (PI) and a perturbation experiment with present-day (mid-1980s) conditions (PD). In the first pair of simulations (GHG), we increase the greenhouse gas concentrations from PI to PD with constant (PD) aerosol concentrations. In the second pair (AP) aerosols are calculated with PD and PI aerosols including the respective aerosol precursor emissions while greenhouse gas concentrations are kept constant at PD levels. In the third pair (GHG–AP) we increase both greenhouse gas concentrations and aerosol emissions from PI to PD. The model is described in the next section followed by a discussion of the climate responses and interpretation of the results.

2. Model description

The atmospheric general circulation model (GCM) used in this study is the fourth-generation Max Planck Institute for Meteorology model, ECHAM4, which has evolved from the European Centre for Medium-Range Weather Forecasts (ECMWF) model (Roeckner et al. 1996). ECHAM4 solves prognostic equations for vorticity, divergence, surface pressure, temperature, water vapor, the sum of cloud water and ice water content, and a number of chemical constituents. The prognostic variables are represented by spherical harmonics with triangular truncation at wavenumber 30 (T30) except for the advection of water vapor, cloud water, and chemical species, which is treated with a flux-form semi-Lagrangian scheme (Rasch and Lawrence 1998). The time step is 30 min for dynamics and physics, except for radiation, which is calculated at 2-h intervals. A hybrid sigma-pressure coordinate system is used with 19 irregularly spaced levels up to a pressure level of 10 hPa. The radiation code has been adopted from the ECMWF model (Morcrette 1991) with a few modifications such as the consideration of additional greenhouse gases [methane, nitrous oxide, and 16 chlorofluorocarbons (CFCs)]. The water vapor continuum has been revised to include temperature-weighted band averages of *e*-type absorption and also a band-dependent ratio of *p*–*e*-type to *e*-type continuum absorption (Giorgetta and Wild 1995). The single-scattering properties of cloud droplets and approximately ''equivalent'' ice crystals are derived from Mie theory with suitable ad-

aptation to the broadband model (Rockel et al. 1991). The effective radii of droplets and ice crystals are parameterized in terms of the liquid and ice water content, respectively. A higher-order closure scheme is used to compute the turbulent transfer of momentum, heat, moisture, cloud water, and chemical species within and above the atmospheric boundary layer. The eddy diffusion coefficients are calculated as functions of the turbulent kinetic energy, which is obtained from the respective rate equation (Brinkop and Roeckner 1995). Vertical fluxes in convective clouds are calculated using the mass flux scheme for penetrative, shallow, and midlevel convection developed by Tiedtke (1989). The cloud water content is calculated from the cloud water transport equation, including sources and sinks due to phase changes and precipitation formation by coalescence of cloud droplets and gravitational settling of ice crystals. Fractional cloud cover is parameterized as a function of relative humidity (Sundquist et al. 1989).

The cloud microphysics scheme implemented in the operational version of ECHAM4 was applied in the simulation GHG and is described in detail in Roeckner et al. (1996). The scheme, which couples the aerosol distributions with the cloud physics as applied in the AP and GHG–AP simulations, is described in Lohmann and Roeckner (1996), Lohmann et al. (1999, 2000), and Lohmann (2002). In these experiments, cloud water and cloud ice are treated separately as prognostic variables and a budget equation for the cloud droplet number concentration and for the ice crystal number concentration are introduced. The bulk microphysics parameterizations for warm phase processes are derived from the stochastic collection equation (Beheng 1994), while the parameterizations of the mixed and ice phase were originally developed for a mesoscale model (Levkov 1992). Parameterized microphysical processes are condensational growth of cloud droplets, depositional growth of ice crystals, homogeneous and heterogenous freezing of cloud droplets, autoconversion of cloud droplets, aggregation of ice crystals, accretion of cloud ice and cloud droplets by snow, aggregation of cloud droplets by rain, evaporation of cloud water and rain, sublimation of cloud ice and snow, and melting of cloud ice and snow. A parameterization of the autoconversion rate of cloud droplets (Beheng 1994) has been introduced, which depends not only on the liquid water content but additionally on the cloud droplet number concentration (CDNC). Cloud droplet nucleation depends on the total number of aerosols at cloud base, the vertical velocity, and an activation parameter (Lohmann et al. 1999) so that changes in aerosol concentration can feed back on the cloud physics and dynamics. The performance of this scheme and the calculated effects of anthropogenic aerosol on cloud forcing are reported upon in Lohmann et al. (2000).

The aerosol model predicts the particle mass mixing ratios of the key components sulfate, black carbon, organic carbon (only primary aerosol), mineral dust, and sea salt and includes emissions, transport, chemical transformations, deposition, sedimentation of coarse mode particles, and removal by precipitation. All aerosol components are assumed to be present in the accumulation mode, with mineral dust and sea salt additionally in the coarse mode.

The sulfur chemistry model treats four sulfur species as prognostic variables: dimethyl sulfide (DMS) and sulfur dioxide (SO_2) as gases, and sulfate (SO_4^{2-}) and methane sulfonic acid (MSA) as aerosol. DMS as well as SO_2 in the gaseous phase are oxidized by reaction with hydroxyl radicals (OH) during the day. Additionally, DMS reacts with nitrate radicals (NO_3) at night. End products of DMS oxidation are SO_2 and MSA. Dissolution of SO_2 within cloud water is calculated according to Henry's law. In the aqueous phase we consider oxidation of SO_2 by hydrogen peroxide (H_2O_2) and ozone (O_3). Three-dimensional monthly mean oxidant concentrations are prescribed based on calculations with ECHAM and a more comprehensive chemical model. Datasets of oxidant distributions have been used as calculated by Roelofs et al. (1998). The calculation of the reaction rates, and of the dissolution and dissociation rates of SO_2, requires assumptions about the pH of cloud water. Hence, we diagnostically estimate the cloud water pH as a function of the sulfate concentrations. The end product of the gaseous and the aqueous phase oxidation of SO_2 is (SO_4^{2-}) [for a more detailed description, see Feichter et al. (1996)]. The performance of the scheme was demonstrated in two model comparisons [Rasch et al. (2000b) and the Comparison of Large-Scale Sulfate Models, COSAM; Barrie et al. 2001; Lohmann et al. 2001; Roelofs et al. 2001].

Sink processes of aerosols are dry deposition at the ground and removal by precipitation. Mineral dust and sea salt coarse-mode particles additionally undergo sedimentation. The dry deposition flux to the ground is assumed to be proportional to both the concentration in the lowest model level (about 30 m above the surface) and to a prescribed dry deposition velocity. The dry deposition velocities for SO_2 are assumed to be 0.6, 0.8, and 0.1 cm s^{-1} over land, water, and snow, respectively, whereas all hygroscopic aerosol [sulfate, MSA, sea salt, and hydrophilic black carbon (BC) and organic carbon (OC)] are deposited by a constant velocity of 0.2 cm s^{-1} (Feichter et al. 1996). Freshly emitted carbonaceous aerosols are assumed to be hydrophobic and are thus removed less efficiently using a dry deposition velocity of 0.025 cm s^{-1}. Precipitation scavenging of aerosols is calculated explicitly in terms of the model's precipitation formation and evaporation rate. Three processes are taken into account, uptake of sulfate, MSA, sea salt, and hydrophilic BC and OC in cloud water or cloud ice by nucleation scavenging, impaction scavenging within the cloud, and collection by falling raindrops or snowflakes below the cloud. We assume that 90% of the aerosol mass becomes incorporated into cloud droplets and 10% of the aerosol mass into ice crystals (A. Floss-

TABLE 1. Physical and optical aerosol properties: mode radius r_m at 0% and 80% relative humidity, respectively, std dev σ of the lognormal distribution and specific density ρ_s; mass extinction efficiency σ_e; single-scattering albedo ω_0; and asymmetry factor g for dry aerosols at 0.5-μm wavelength according to Hess et al. (1998).

Species	r_m 0% RH (μm)	r_m 80% RH (μm)	σ (μm)	ρ_s (g cm^{-3})	σ_e (m^{-2} g^{-1})	ω_0	g
Sulfuric acid	0.0695	0.118	2.03	1.7	3.8	1.0	0.77
Organic carbon	0.0212	0.031	2.24	1.8	3.6	0.98	0.68
Black carbon	0.0118	0.0118	2.00	2.3	11.0	0.23	0.35
Mineral dust (accumulation)	0.39	0.39	2.00	2.6	0.55	0.83	0.76
Sea salt (accumulation)	0.209	0.416	2.03	2.2	1.3	1.0	0.78

mann 1995, personal communication), except for hydrophobic BC and OC, which are not subject to in-cloud scavenging. A fraction of the aerosol incorporated in cloud droplets and ice crystals is removed from the grid box in proportion to the precipitation formation rate. Below cloud scavenging is parameterized depending on the precipitation flux, aerosol mass mixing ratio in the respective grid boxes, and a collection efficiency assumed to be 0.3 (Berge 1993). If cloud water or precipitation evaporates, the aerosol mass is released again into the atmosphere.

Aerosol number concentrations are derived from the predicted aerosol mass mixing ratios by prescribing physical properties for each component assuming that the different aerosols are externally mixed. Each aerosol type is described by the specific density, the mode radius, and the width of the assumed lognormal distribution. These data have been derived from observations by Hess et al. (1998). The optical properties for each component, for the model's radiative spectral intervals, and for different classes of ambient relative humidity have been calculated based on Mie theory (Hess et al. 1998). These physical and optical aerosol properties are given in Table 1. Radiative forcings of the direct aerosol effect based on these properties have been calculated for sulfate aerosols by Feichter et al. (1997), for black carbon by Cooke et al. (1999), and for a mixture of both aerosol components by Lohmann and Feichter (2001).

The emission inventories and source strengths used in this study are shown in Table 2. We consider sulfur and OC emissions from biogenic sources and sulfur from background volcanic activity as well as anthropogenic sulfur, BC and OC emissions from biomass burning, fossil fuel use, and industrial activities. All biogenic sulfur emissions from the ocean, soils, and plants are assumed to occur as DMS whereas volcanic and anthropogenic sulfur emissions are assumed to occur as SO_2. DMS fluxes are calculated from the DMS ocean surface concentrations as given by Kettle et al. (1999) calculating the air–sea gas exchange depending on the sea surface temperature and 10-m wind (Liss and Merlivat 1986). All emissions from biomass burning are assumed to be anthropogenic. The SO_2 source of 66 Tg yr^{-1} due to fossil fuel combustion and industrial activities is from the Global Emissions Inventory Activity (GEIA/IGAC; Benkovitz et al. 1994) and is representative for the year 1985. The global sulfur emissions amount to 94 Tg yr^{-1}, of which 70% can be ascribed to anthropogenic sources. Carbonaceous aerosol (BC and primary OC) emissions from fossil fuel use were taken from Cooke et al. (1999) and emissions due to biomass burning are from Liousse et al. (1996). These emissions are representative for the early 1980s. Carbonaceous aerosols may be predominantly hydrophobic but due to condensation of condensable matter on the aerosol surface they become hydrophilic with time. We assume that 80% (50%) of the freshly emitted BC (OC) is hydrophobic and 20% (50%) hydrophilic. Hydrophobic particles become hydrophilic with a characteristic aging time of 1 day (Cooke et al. 1999). Biogenic OC emissions from vegetation are taken from Guenther et al. (1995). We assume that a fraction of 11% forms particulates (Penner et al. 2002). Carbonaceous aerosol emissions amount to 97 Tg yr^{-1}, of which 82% is anthropogenic. Monthly mean mineral dust sources of accumulation and coarse-mode particles are taken from Ginoux et al. (2001). The generation of accumulation and coarse-mode sea salt particles is calculated depending on the model's 10-m wind according to a parameterization of Monahan et al. (1986).

The atmospheric GCM is coupled to a dynamically passive slab ocean model with a depth of 50 m (Roeckner et al. 1995). The temperature of the slab ocean is calculated from the net heat flux at the surface provided

TABLE 2. Annual and global mean source strengths.

Compound	Natural and anthropogenic	Anthropogenic
Sulfur total (Tg yr^{-1}),	94	66
volcanoes,	8	
DMS	20	
Black carbon (Tg yr^{-1})	14	14
Organic carbon (Tg yr^{-1}; primary particles)	97	80
Mineral dust		
Accumulation mode	380	
Coarse mode	620	
Sea salt		
Accumulation mode	18	
Coarse mode	1250	

TABLE 3. Calculated annual mean budgets of the total anthropogenic aerosol burden and the mass fraction of black carbon (BC) particles.

	Burden (Tg S/C)		BC of total anthropogenic aerosol load (%)	
	AP	GHG–AP	AP	GHG–AP
Global	2.49	2.01	11	11
NH	1.76	1.39	12	11
NH land	0.96	0.83	17	13

by the atmospheric GCM. To account for model errors and for the missing part of the thermodynamic budget, a correction term is calculated from an uncoupled model experiment where the sea surface temperature (SST) is specified according to the observed climatology. A similar procedure is applied to the thermodynamic sea ice model, so that the model is able to reproduce the observed seasonal variation of SST and sea ice extent. For achieving climate equilibrium, the model was integrated for 10 (GHG), 20 (AP), and 25 yr (GHG–AP), respectively. The simulations were then extended for another 20 (GHG) and 50 yr (AP, GHG–AP), respectively, and results for these comparatively long periods are presented as the respective differences (PD − PI) of the multiyear averages. According to their design, equilibrium experiments cannot reproduce the observed time evolution of climate change but are useful tools for exploring the effects of a specific perturbation to the climate system.

3. Results

a. Aerosol yield and atmospheric burden

Table 3 summarizes the global and Northern Hemisphere (NH) budgets of the anthropogenic aerosol burden (PD − PI) for the AP and GHG–AP simulations. Although we applied the same source strength and distribution in the AP and the GHG–AP scenario, the total aerosol load in the AP scenario is higher than that in the combined scenario. In the AP simulation the anthropogenic sulfate and carbonaceous particle load amounts to 2.5 Tg C/S (teragrams of carbon and sulfate, respectively) globally compared to 2.0 Tg C/S in the GHG–AP simulation. In both scenarios 11% of the total aerosol mass is BC whereas the BC mass fraction is somewhat higher closer to the sources, as for instance over the NH continents because BC is emitted as a primary particle. There is a strong seasonal variation in atmospheric aerosol load (not shown): in boreal winter, the NH contributes 81% and 78% to the global total aerosol load in the AP and GHG–AP scenarios, respectively. On the other hand, in boreal summer, during the Southern Hemisphere (SH) biomass-burning season, the NH contributes only 55% and 51% to the global load in the AP and GHG–AP scenarios, respectively. Changes in the mineral dust and sea salt load due to changes in the wind fields are relatively small. However, we would expect stronger changes in the mineral dust load if we had calculated the sources interactively rather than using prescribed emission fluxes. As shown in Figs. 1a and 1b, the annual mean aerosol burden is highest over the highly industrialized regions of Southeast Asia and Europe and over central Africa due to high biomass-burning emissions. Reasons for the substantial differences between GHG–AP (Fig. 1a) and AP (Fig. 1b) are discussed in section 3e.

The global mean aerosol optical depth (AOD) at 0.55 μm amounts to 0.053 in the AP and 0.032 in the GHG–AP scenarios. Typical calculated NH continental AODs are between 0.1 and 0.3 and up to 0.5 in highly polluted regions (cf. Figs. 1c and 1d). A comparison of the calculated mass distribution and the optical depth (GHG–AP scenario) with other model results and with remote sensing data can be found in Kinne et al. (2003). In general, the model simulates lower AODs than those retrieved from various satellite data sources, which is mainly caused by assuming too large aerosol mode radii (Lohmann and Lesins 2002). The model-calculated AODs are lower by about 30%–50% over the source regions and by a factor of 2 over remote oceanic regions. The latter bias is additionally caused by an underestimate of the sea salt aerosol optical depth and may not affect our conclusions about the anthropogenic aerosol effects.

b. Temperature

As shown in Table 4, the direct and indirect anthropogenic aerosol effects in the AP experiment cause a global annual mean cooling of almost 0.9 K. Consistent with the spatial distribution of anthropogenic emissions, the cooling is larger in the NH than in the SH and larger over the continents than over the oceans. In the GHG experiment, the land–sea contrast in the warming is also evident, while the interhemispheric difference, that is, the NH–SH ratio, is less pronounced than in AP due to the longer lifetime of greenhouse gases compared to aerosols. In the combined simulation, GHG–AP, the global warming is calculated as 0.6 K.

The zonal annual mean changes in surface air temperature are shown in Fig. 2 separately for sea (including areas covered with sea ice) and land. The response amplifies at high latitudes over the oceans and at high and midlatitudes over land, which is caused by positive feedbacks between changes in temperature and snow/ice cover, respectively, while the response between 30°S and 30°N is more uniform. In the combined experiment, GHG–AP, a warming is simulated at all latitudes. Here, due to partial compensation of the individual responses, the interhemispheric differences are moderate (cf. Table 4). The spatial patterns of annual temperature change are shown in Fig. 3. In AP (Fig. 3a), a cooling is simulated everywhere. Local peaks of up to 3 K are found downwind of highly industrialized regions such as the

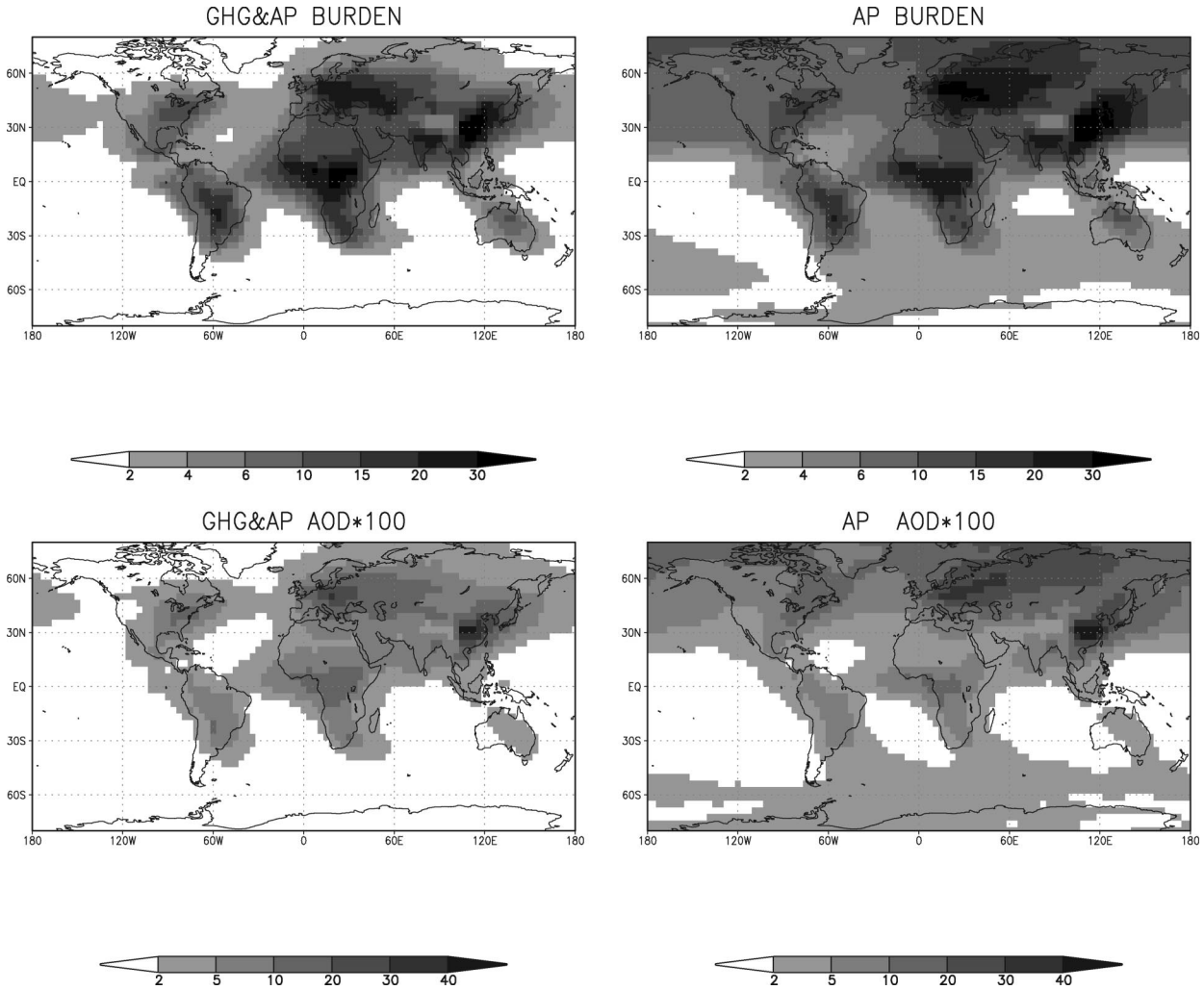

FIG. 1. (top) Annual mean aerosol burden (mg m^{-2}) and (bottom) aerosol optical depth from anthropogenic emissions as calculated in scenario (left) GHG + AP and (right) AP.

eastern United States (cf. Fig. 2a, solid line) but also in regions with seasonal snow cover. On the other hand, the cooling is small in less polluted remote regions as, for example, the SH oceans (cf. Fig. 1b). Seasonal effects are evident in biomass-burning regions with local cooling of about 1 K (not shown). The temperature changes in AP are significant at the 95% level (Student's *t* test) in all industrialized regions affected by anthropogenic pollution and also over regions affected by biomass burning. As noted above, the interhemispheric differences are significantly smaller in GHG (Fig. 3b) than in AP, while other features such as the land–sea contrast and high-latitude amplification of the response are simulated as well. In GHG–AP (Fig. 3c), warming prevails but in some areas the aerosol effects are large enough to practically offset or even reverse the greenhouse warming. This is found not only over land (eastern Europe, Southeast Asia, central Africa, and parts of South America) but also over a few oceanic regions. In conjunction with the strong Arctic cooling in AP, NH sea ice cover increases by about 25% in summer while snow cover increases over western Siberia and eastern Canada in winter (not shown). A similar result was obtained by Williams et al. (2001) who studied the indirect sulfate aerosol effect using the Hadley Center model. In GHG, on the other hand, anomalous melting of sea ice is evident in the North Atlantic sector, in particular, while hardly any change in NH sea ice cover is found in the combined experiment, GHG–AP.

TABLE 4. Annual mean surface temperature differences between present-day and preindustrial simulations in (K).

	Global	NH land	NH ocean	SH land	SH ocean
AP	−0.87	−1.38	−0.97	−0.87	−0.56
GHG	1.72	2.47	1.57	1.99	1.41
GHG–AP	0.57	0.65	0.46	0.65	0.60

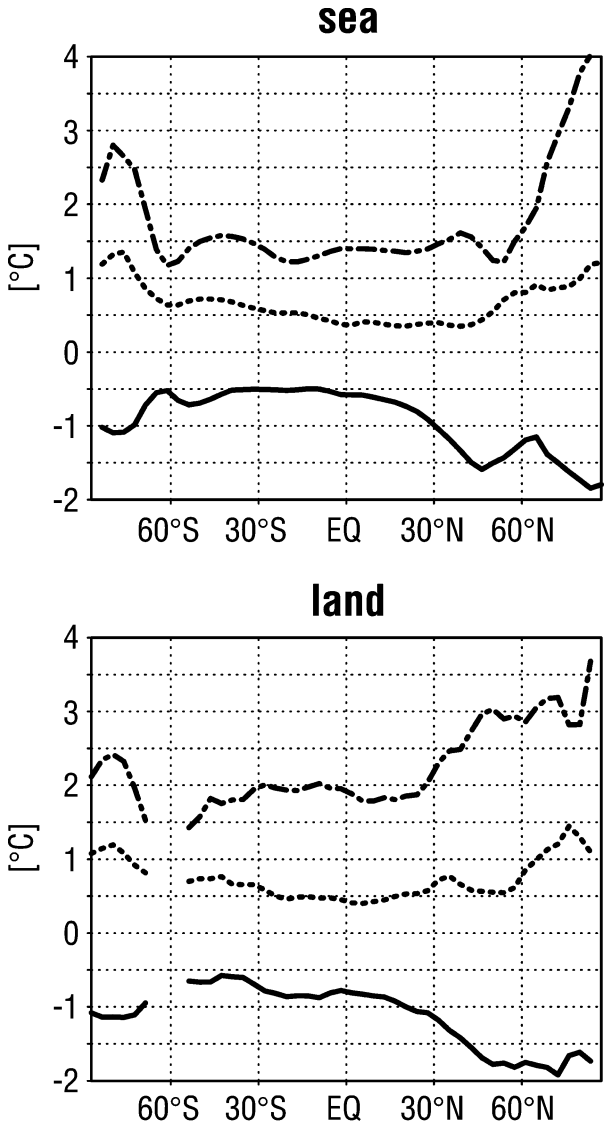

FIG. 2. Zonal and annual mean surface temperature differences (K) between the PD and PI simulations for the AP (solid line), GHG (dashed–dotted line), and GHG–AP (dotted line) simulations.

c. Hydrological cycle

Aerosols change the surface radiation budget through reflection and absorption of solar radiation in the atmospheric layer, where they are most abundant. The global and annual mean reduction in net surface solar radiation is 2.9 W m^{-2} in AP, 1.4 W m^{-2} in GHG, and 3.8 W m^{-2} in GHG–AP. According to Table 5, cloud cover changes are small. However, the increase in cloud water path (CWP) in all three experiments contributes to the reduction in surface solar radiation, but the impact on the hydrological cycle is different. In GHG, the relatively modest decrease in solar radiation is overcompensated by enhanced downwelling longwave radiation from the atmosphere so that the change in net surface radiation becomes positive (1.6 W m^{-2}). This is balanced by anomalous cooling through increased sensible and latent heat fluxes. Consequently, as shown in Table 5, both evaporation and precipitation are enhanced by 0.08 mm day^{-1} in the global annual mean. In AP, the substantial CWP increase is caused by the second indirect effect through reduced precipitation formation and, hence, longer cloud lifetime. In contrast to GHG, the radiative forcing of aerosols is basically felt at the surface. Therefore, changes in surface energy fluxes due to increasing aerosol load are larger than in a GHG experiment with the same global mean radiative forcing (Allen and Ingram 2002, and references therein). This is confirmed in Table 5, which shows that the changes in evaporation and precipitation are larger in AP than in GHG although both the forcing and the temperature change are smaller than in GHG.

Table 6 shows the sensitivity of a few hydrological parameters normalized by the change of the global annual mean surface air temperature. These normalized changes are different in the three experiments, indicating a substantial dependency on the type of forcing. This applies to the water vapor content and, in particular, to the cloud water path and to evaporation and to precipitation. The hydrological sensitivity in AP, defined as the global precipitation change (in %) normalized by the global surface temperature change, is almost three times higher than in GHG (1.5% K^{-1}), which is just slightly smaller than the 1.9% K^{-1} given in the Intergovernmental Panel on Climate Change's Third Assessment Report (IPCC TAR) as an average of 15 models (Cubasch et al. 2001). This threefold difference is the main reason why the hydrological sensitivity in GHG–AP has a negative sign; that is, the global warming is associated with a decrease in global evaporation and precipitation: while the warming due to increasing greenhouse gases tends to enhance the hydrological cycle, the aerosol effects on the surface radiation budget are large enough to reverse this effect. A negative hydrological sensitivity was also found by Roeckner et al. (1999) in transient scenario experiments including GHG forcing, and the direct and the first indirect aerosol effects of anthropogenic sulfate.

The residence time of water vapor in the atmosphere, defined as the ratio of total precipitable water to precipitation, increases in all three experiments; that is, the relative changes in atmospheric water vapor are larger than those in precipitation. While the former are governed largely by the Clausius–Clapeyron relationship given that the relative humidity is approximately unchanged (Allen and Ingram 2002), the latter are additionally constrained by changes in the surface energy budget (Boer 1993). This explains why the change in residence time is smaller in AP, with comparatively large changes in both surface solar radiation and precipitation, than in GHG. In GHG–AP, the aerosol effects on the surface radiation budget and, therefore, precipitation are large enough to virtually offset the GHG effects at the surface (cf. Table 5) so that the increase in residence

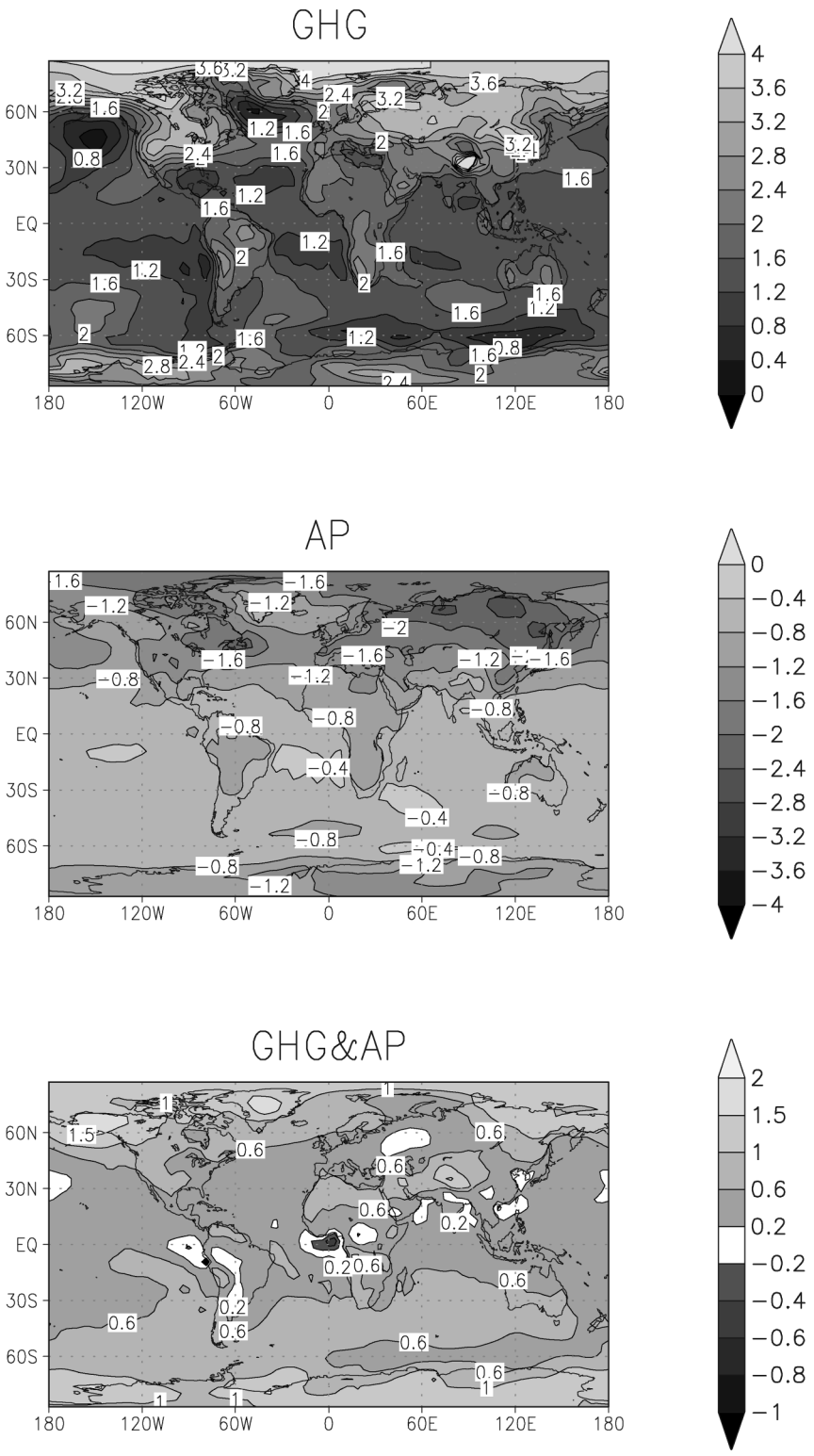

FIG. 3. Annual mean surface temperature differences (K) between PD and PI as calculated in the three scenarios.

TABLE 5. Annual mean differences between present-day and preindustrial simulations and percentage change PC in % [(PD − PI)100/PD]. (Note: the cloud water path represents the liquid and the solid phase.)

		Global	NH land	NH ocean	SH land	SH ocean
GHG	Evaporation (mm day^{-1}),	0.08	0.05	0.07	0.07	0.08
	PC	2.8	3.9	2.5	3.9	2.4
	Precipitation (mm day^{-1}),	0.07	0.09	0.06	0.13	0.07
	PC	2.5	4.7	1.8	5.1	2.3
	Cloud cover fractional %,	−0.4	−0.9	−0.3	−0.4	−0.2
	PC	−0.6	−1.6	−0.4	−0.8	−0.3
	Cloud water path (g m^{-2}),	4.2	4.2	4.5	2.2	4.3
	PC	5.0	7.1	4.8	3.4	4.7
AP	Evaporation (mm day^{-1}),	−0.11	−0.12	−0.15	−0.09	−0.08
	PC	−3.5	−8.2	−3.8	4.2	2.3
	Precipitation (mm day^{-1}),	−0.11	−0.17	−0.16	−0.16	−0.04
	PC	−3.5	−7.7	−4.3	−5.2	−1.3
	Cloud cover fractional %,	0.7	1.1	0.9	0.4	0.5
	PC	1.1	1.9	1.3	0.7	0.7
	Cloud water path (g m^{-2}),	8.7	8.4	12.7	8.5	5.6
	PC	10	13	13	14	6
GHG–AP	Evaporation (mm day^{-1}),	−0.03	−0.04	−0.06	−0.01	−0.01
	PC	−1.1	−3.1	−1.8	−0.6	−0.3
	Precipitation (mm day^{-1}),	−0.03	−0.06	−0.07	−0.04	0.01
	PC	−1.1	−3.2	−2.2	−1.6	−0.4
	Cloud cover fractional %,	0.02	−0.1	0.06	0.3	0.00
	PC	0.03	−0.2	0.09	0.7	0
	Cloud water path (g m^{-2}),	11.0	12.5	13.2	14.2	7.9
	PC	11	17	11	16	8

time is governed essentially by the increase in atmospheric water vapor caused by global warming. Due to different impacts of aerosols and greenhouse gases on the radiation budget of the atmosphere and the surface, the response of the hydrological cycle to aerosol forcing is not just a mirror image of that to greenhouse gas forcing.

The zonal and annual mean precipitation changes are shown in Fig. 4. In AP precipitation decreases particularly in regions with large aerosol loads, such as high northern latitudes and tropical continents, for example, while small changes are found at middle and high southern latitudes. Since precipitation is the main sink of particles, a positive feedback exists with high aerosol load producing low precipitation and thus enhancing the aerosol load and its effect on temperature and precipitation. Additionally, aerosol cooling of the earth's surface stabilizes the boundary layer and suppresses convection. This is particularly evident over tropical continents where mean precipitation is high and biomass burning affects the surface radiation budget. In GHG, the changes are predominantly positive with the highest values in the Tropics and at higher latitudes. In the combined experiment, GHG–AP, despite a general warming (cf. Fig. 3c), precipitation is decreasing at most latitudes. This is more pronounced over the continents, especially at lower latitudes, than over the oceans. Precipitation tends to increase at higher latitudes, especially in regions where the aerosol load is small, such as the region around Antarctica (cf. Fig. 1a).

The spatial distributions of the annual mean precipitation changes are shown in Fig. 5. In AP (Fig. 5a), the pattern bears some resemblance to that of the anthropogenic aerosol load (cf. Fig. 1b) with decreases simulated over the eastern United States, Europe, and Southeast Asia, and also over tropical continents (South America, Africa) where biomass burning is the main aerosol source. Little change is found over the SH oceans, except for the patterns caused by shifts in the convergence zones in the tropical Pacific. However, not

TABLE 6. Annual and global mean climate response in % [(PD − PI)/PI] normalized by the change of the global mean surface temperature.

	Temperature (K)	Water vapor content (% K^{-1})	Evaporation and precipitation (% K^{-1})	Cloud water path (% K^{-1})	Total cloud cover (% K^{-1})	Atmospheric residence time of precipitable water (% K^{-1})
AP	−0.87	5.7	3.9	−13.0	−1.3	4
GHG	+1.7	7.8	1.5	+3.1	−0.3	8
GHG–AP	+0.57	7.8	−1.9	+22.0	0.1	10

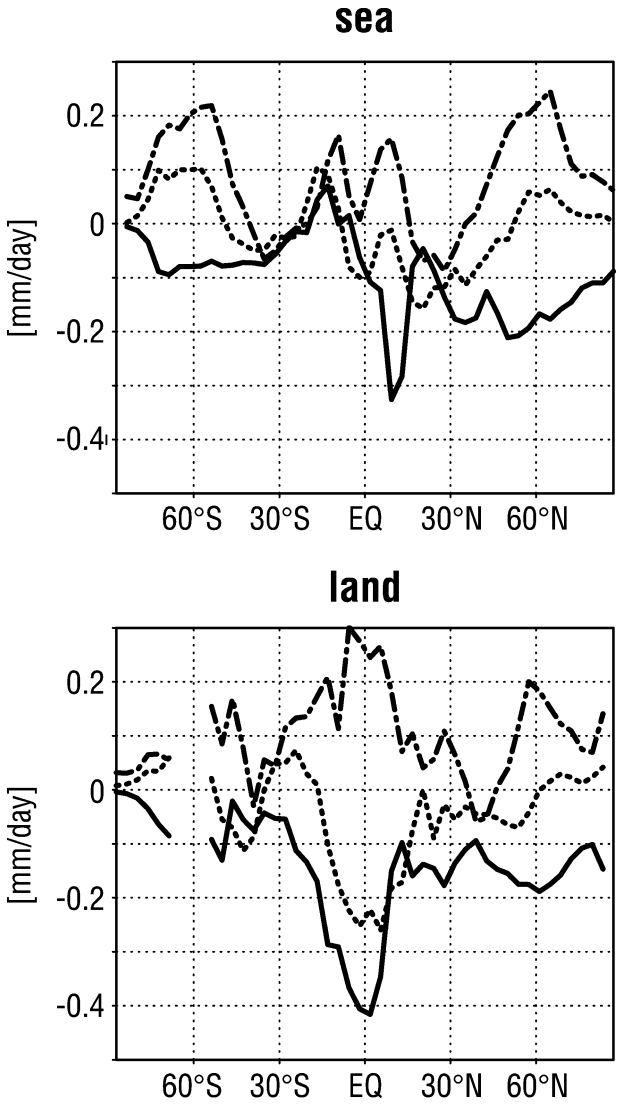

FIG. 4. Zonal and annual mean precipitation differences (mm day^{-1}) between the PD and PI simulations for the AP (solid line), GHG (dashed–dotted line), and GHG–AP (dotted line) simulations.

all of the changes can simply be explained by changes in aerosol load. This might be inferred from Fig. 5b, which shows the pattern for the GHG experiment. Although the GHG forcing is spatially more uniform than the AP forcing, there is some similarity with AP, except for the sign. For example, precipitation increases (decreases) at high northern latitudes in GHG (AP), the tropical Pacific pattern is not very dissimilar but of different sign, and increased (decreased) precipitation is simulated in Southeast Asia and also over tropical South America and Africa. These similarities can partly be explained by the thermal land–sea contrast in AP and GHG (cf. Figs. 2 and 3), which tends to dampen (strengthen) the monsoons in AP (GHG). The most obvious difference between AP and GHG can be found over the Southern Ocean where the GHG response is much more pronounced than that of AP. This is consistent with the respective changes in temperature (cf. Figs. 3a,b). Moreover, in GHG, there is a northward shift of the high-precipitation belt associated with cyclonic activity. This results in drier conditions between 30° and 45° and wetter conditions between 45° and 60°, while aerosol cooling in AP reduces precipitation at middle and high northern latitudes. In the combined experiment (Fig. 5c), despite a general warming, precipitation decreases predominantly over those regions where aerosol effects are large enough to practically offset the greenhouse warming (cf. Fig. 3c). This applies to regions like Europe, tropical continents with adjacent oceans, Southeast Asia, and parts of the Indian Ocean and the China Sea, whereas small changes or slight increases are simulated in oceanic regions with relatively low aerosol load (cf. Fig. 1a).

d. Nonlinear effects

Based on a transient climate change experiment, Haywood et al. (1997) concluded that the spatial distributions of changes in surface air temperature and precipitation can be approximated by adding the individual responses from a greenhouse warming and aerosol cooling experiment, respectively. To test this hypothesis, the changes in surface air temperature and precipitation in the combined experiment (GHG–AP) are compared with those obtained by adding the individual changes (GHG + AP). According to Table 4, the global warming in the combined experiment (0.57 K) is substantially smaller than the sum of GHG and AP (0.85 K). This difference is largely due to the changes in cloud water path (cf. Table 6) and, hence, in net cloud radiative forcing, which is significantly larger in GHG–AP (-1.5 W m^{-2}) than in AP (-0.3 W m^{-2}) or GHG (-0.1 W m^{-2}). For global precipitation (cf. Table 5), on the other hand, the changes are identical (-0.03 mm day^{-1} in both cases). The respective zonal means are shown in Fig. 6 separately for sea and land. With respect to surface air temperature (Figs. 6a,c) a linearity of the responses cannot be confirmed: at almost all latitudes, the GHG–AP response is significantly smaller than that of GHG + AP, and in addition the shapes of the distributions are dissimilar. Relatively small differences are found at high southern latitudes. The cooling in GHG + AP around 50°N is related to circulation changes in GHG producing local minima in parts of the North Pacific and in the Labrador Sea (cf. Fig. 3b). More similar are the precipitation changes shown in Figs. 6b and 6d. The broadscale patterns agree reasonably well but local differences can be quite large. A comparison of the zonal mean precipitation changes in Fig. 4 shows that the GHG–AP response is essentially governed by aerosol effects, that is, the patterns of AP and GHG–AP are similar, while the GHG forcing tends to mitigate the AP effect. This is also consistent with the result that the hydrological sensitivity to aerosol forcing is almost

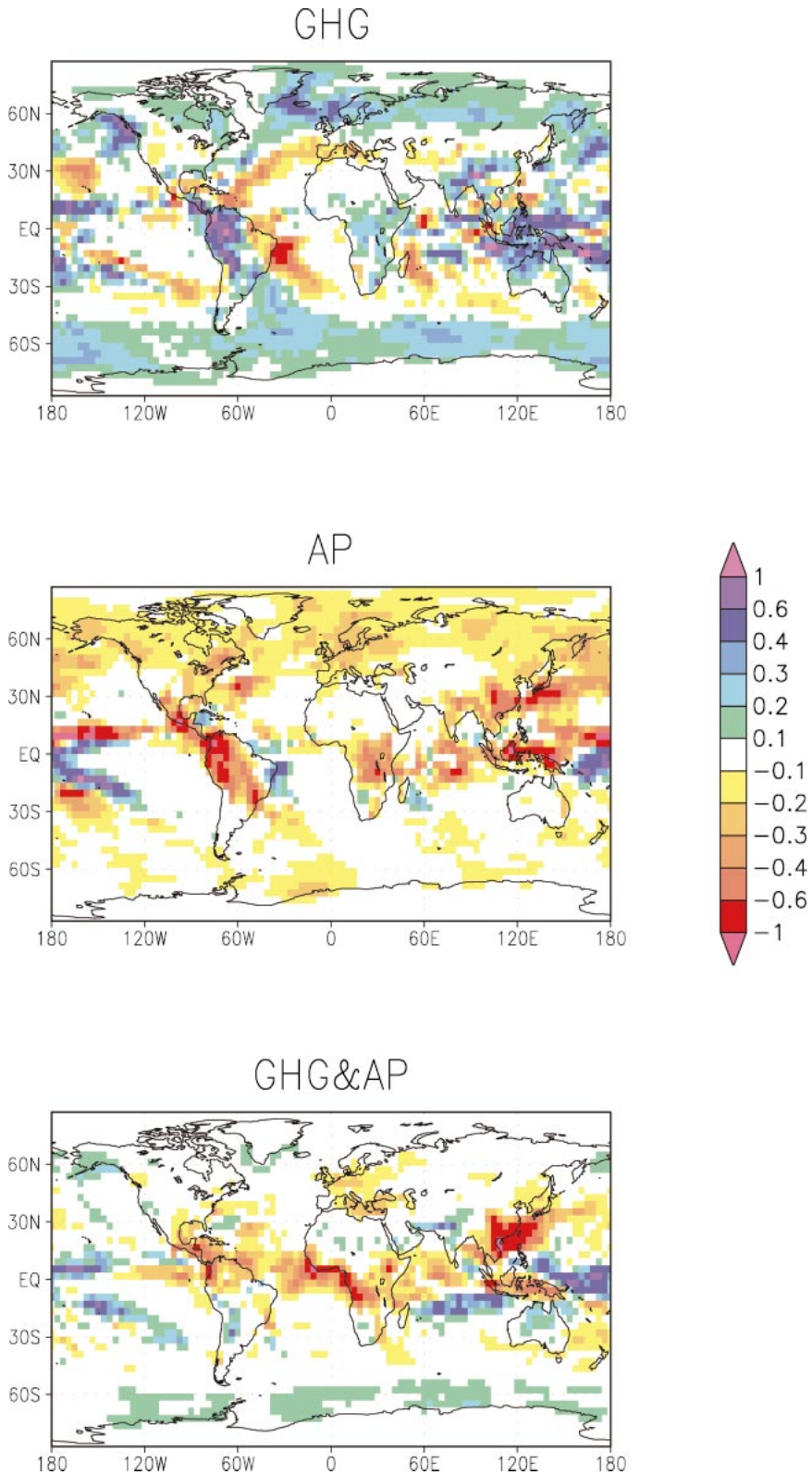

FIG. 5. Annual mean precipitation differences (mm day^{-1}) between PD and PI as calculated in the three scenarios.

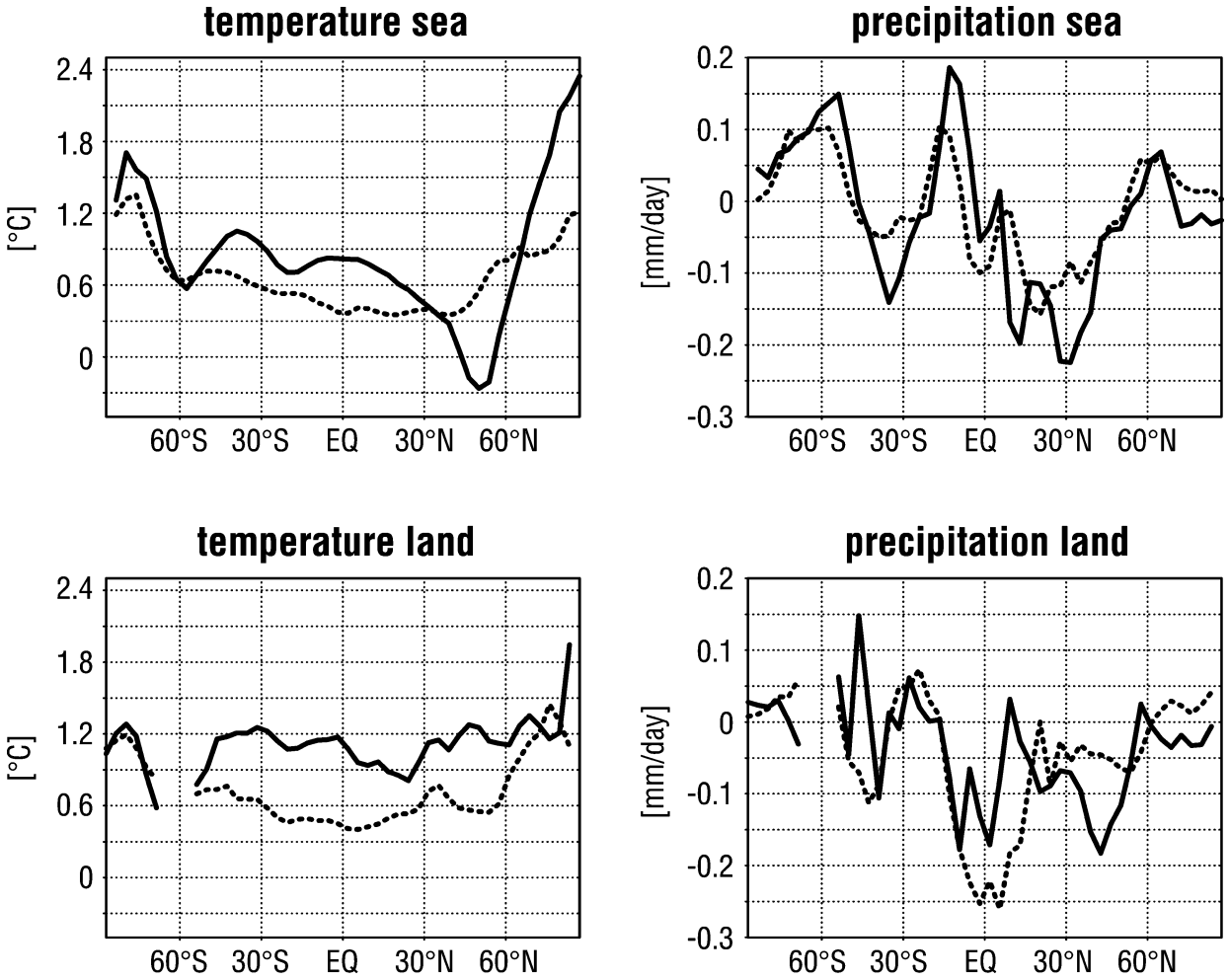

FIG. 6. Zonal and annual mean temperature (K) and precipitation (mm day^{-1}) differences between the PD and PI simulations for the GHG–AP simulation (dotted line) and the sum of the AP and the GHG simulations (solid line).

three times higher than is that to greenhouse gas forcing (cf. Table 6). Based on these results, the hypothesis of Haywood et al. (1997) that the combined precipitation response can be obtained by adding the individual response can only be partially confirmed. The reason could be that Haywood et al. applied a prescribed aerosol distribution, thus neglecting feedback processes between aerosol load and changes in temperature, clouds, and the hydrological cycle.

e. Aerosol–climate interactions

As shown in Figs. 1a and 1b the anthropogenic aerosol load depends crucially on the climate state. In the cooler AP climate, the same source strength results in a higher total aerosol load compared to the warmer GHG–AP climate. Because the total aerosol amount released into the atmosphere is the same in both scenarios, the difference in the atmospheric aerosol yield is attributed to a longer residence time in the AP scenario. For instance, the mean residence time of sulfate is only 3 days in the present-day GHG–AP but 5.6 days in the present-day AP scenario. The reduced aerosol lifetime in the warmer climate constitutes a positive aerosol–temperature feedback. The longer residence time of aerosols allows particles to also pass the NH midlatitude rainbelt and to increase the aerosol load in the Arctic regions. Thus the largest differences occur at high northern latitudes where the aerosol load is considerably higher in the AP experiment (cf. Figs. 1a,b). Numerous processes control the atmospheric residence time of the aerosol and could be responsible for this aerosol–temperature feedback. An increase in aerosols reduces the precipitation efficiency of warm clouds leading to an increase in cloud cover and liquid water path. The resulting longer lifetime of clouds in turn increases the residence time of the aerosols (aerosol lifetime effect). However, this effect is also taken into account in the GHG–AP simulation. The reason for the different aerosol residence times is that over the middle- and high-latitude NH continents, where the main aerosol sources are, the increase in the CWP is smaller in the GHG–

AP simulation than in the AP simulation (not shown). Furthermore, precipitation at NH high latitudes in the AP simulation is reduced, associated with a decrease in the aerosol removal rate, while precipitation changes over NH midlatitudes in the GHG–AP simulation are small (see Fig. 5). The reduced precipitation rate in the AP scenario over the NH midlatitude continents increases the lifetime of clouds and subsequently the cloud water path and the aerosol load. Thus the relationship between source strength and aerosol load is not linear but depends on the climate state.

4. Summary and conclusions

In a series of equilibrium experiments we calculated the climate response to radiative forcings of anthropogenic greenhouse gases (experiment GHG), aerosol particles (experiment AP), and the combination of both greenhouse gases and aerosols (GHG–AP). The study was performed with a coupled model system consisting of the atmospheric circulation model ECHAM4-T30, a mixed layer ocean, and a thermodynamic sea ice model. The atmospheric model includes a transport scheme for chemical constituents, a sulfur chemistry model that calculates sulfate production in the gas and the aqueous phases, and an aerosol model that accounts for source and sink processes. Aerosol particle concentrations affect the radiative fluxes and the formation of cloud droplets at cloud base thus providing a mechanistic link between the aerosol population and cloud properties like cloud albedo and autoconversion rate. Hence, the aerosol cycle, the hydrological cycle, and the atmospheric dynamics are fully and interactively coupled. All three scenarios were calculated twice, once representing greenhouse gas and/or aerosol forcing of preindustrial times and once more for present-day (mid-1980s) conditions. The main results are as follows.

1) In the global annual mean, an increase of surface air temperature by 1.7 K is simulated in GHG, with a decrease of 0.9 K in AP, and an increase in GHG–AP of 0.6 K.
2) Regionally, the greenhouse gas warming in the combined GHG–AP simulation is partially offset by the aerosol effect and is negligibly small in highly polluted areas whereas a warming of more than 1.5 K is simulated over remote regions like Alaska, Greenland, eastern Siberia, and central Asia. Surface temperature changes over the ocean are slightly positive (0.2–0.4 K) downwind of the most industrialized regions in the North Atlantic and North Pacific while the warming over the SH oceans is generally larger than 0.5 K. In GHG, interhemispheric differences are much smaller than are those in AP, where regional aerosol forcing is reflected in the temperature response.
3) In contrast to greenhouse gases, the radiative effect of aerosols is mainly felt at the earth's surface. This has implications for the global hydrological cycle, which is almost three times more sensitive to changes in aerosols than to changes in greenhouse gases. As a result, the global precipitation in the combined experiment (GHG–AP) decreases in conjunction with global warming; that is, the hydrological sensitivity is negative. A strong dependency of the response to the type of forcing has also been found for the total cloud water content and, consequently, for the change in net cloud radiative forcing, which is substantially larger in the combined forcing experiment (-1.5 W m^{-2}) than in either of the other experiments (-0.1 W m^{-2}) in GHG and -0.3 W m^{-2} in AP). Therefore, the global warming in GHG–AP is significantly smaller (0.57 K) than that obtained by adding the individual changes (0.85 K).
4) Applying the same present-day aerosol source strength and distribution, a lower aerosol load is obtained in the warmer simulation (GHG–AP) than in the colder one (AP). In a cooler climate the damping of the hydrological cycle is associated with a longer atmospheric residence time of aerosol particles and a subsequent enhanced spatial spread out. The increase in the atmospheric aerosol load is also accompanied by the longer residence time of clouds due to the second indirect aerosol effect or aerosol lifetime effect. The simulated aerosol load at the same source strength decreases by 17% K^{-1} warming due to greenhouse gases as inferred from the difference between the AP and GHG–AP scenario. A consequence of this aerosol–temperature feedback could be that a further increase in greenhouse gas concentrations reduces the aerosol yield even if the source strength does not change. Hence, an important conclusion is that according to our simulations the climate response to changing aerosol particle concentrations depends on concurrent changes of the state of the atmosphere and the hydrological cycle. Thus, results of climate response studies on the effects of single aerosol compounds or single mechanisms should be regarded with caution. Thus, the aerosol–temperature feedback as described here may help explain the massive dust content in the atmosphere during glacial periods (e.g., Mahowald et al. 1999). It is speculated that the dust load may have been enhanced by larger dust source areas (Chylek et al. 2001), changes in near-surface winds, and, possibly, also by the longer residence time of aerosol particles in a cooler climate.

Although our model is relatively complex compared to most others applied in climate change experiments so far, it has a number of shortcomings. First, for computational efficiency, we used a relatively coarse spatial resolution so the regional details of the responses should be viewed with caution. Second, important aerosol components like nitrate and secondary organics are not yet considered and, third, large uncertainties exist with re-

spect to the biomass-burning sources: we neither know the source strength and the distribution of specific years nor the physical and optical properties of the different source types. Moreover, one of the weaknesses of all current climate models including this one is the still rather crude representation of clouds.

Due to the equilibrium mode of operation, a comparison between simulated and observed climate change is beyond the scope of this study. Nevertheless, our study seems to support the view that climate change simulations will only be meaningful if interactions between aerosol physics, chemistry, and cloud physics are considered in conjunction with greenhouse forcing.

Acknowledgments. The research was supported by the German ministry BMBF within the AFS project.

REFERENCES

Ackerman, A. S., O. B. Toon, D. E. Stevens, A. J. Heymsfield, V. Ramanathan, and E. J. Welton, 2000: Reduction of tropical cloudiness by soot. *Science,* **288,** 1042–1047.

Albrecht, B. A., 1989: Aerosols, cloud microphysics, and fractional cloudiness. *Science,* **245,** 1277–1230.

Allen, M. R., and W. J. Ingram, 2002: Constraints on future changes in climate and the hydrologic cycle. *Nature,* **419,** 224–232.

Barrie, L., and Coauthors, 2001: A comparison of large scale atmospheric sulphate aerosol models COSAM: Overview and highlights. *Tellus,* **53B,** 615–645.

Beheng, K., 1994: A parameterization of warm cloud microphysical conversion processes. *Atmos. Res.,* **33,** 193–206.

Benkovitz, C. M., C. M. Berkowitz, R. C. Easter, S. Nemesure, R. Wagener, and S. E. Schwartz, 1994: Sulfate over the North-Atlantic and adjacent continental regions—Evaluation for October and November 1986 using a 3-dimensional model-driven by observation-derived meterology. *J. Geophys. Res.,* **99** (D10), 20 725–20 756.

Berge, E., 1993: Coupling of wet scavenging of sulfur to clouds in a numerical weather prediction model. *Tellus,* **45B,** 1–22.

Boer, G. J., 1993: Climate change and the regulation of the surface moisture and energy budgets. *Climate Dyn.,* **8,** 225–239.

Brinkop, S., and E. Roeckner, 1995: Sensitivity of a general-circulation model to parameterizations of cloud–turbulence interactions in the atmospheric boundary-layer. *Tellus,* **47A,** 197–220.

Charlson, R. S., and M. J. Pilat, 1969: Climate: The influence of aerosols. *J. Appl. Meteor.,* **8,** 1001–1002.

Chylek, P., and J. A. Coakley, 1974: Aerosols and climate. *Science,* **183,** 75–77.

——, G. Lesins, and U. Lohmann, 2001: Enhancement of dust source area during past glacial periods due to changes of the Hadley circulation. *J. Geophys. Res.,* **106** (D16), 18 477–18 485.

Cooke, W. F., C. Liousse, H. Cachier, and J. Feichter, 1999: Construction of a 1° × 1° fossil fuel emission dataset for carbonaceous aerosols and implementation into the ECHAM4 model. *J. Geophys. Res.,* **104,** 22 137–22 162.

Cubasch, U., and Coauthors, 2001: Projections of future climate change. *Climate Change 2001: The Scientific Basis,* J. T. Houghton et al., Eds., Cambridge University Press, 525–582.

Dai, A., A. D. DelGenio, and I. Y. Fung, 1997: Clouds, precipitation and temperature range. *Nature,* **386,** 665–666.

Douville, H., F. Chauvin, S. Planton, J. F. Royer, D. Salas-Melia, and S. Tyteca, 2002: Sensitivity of the hydrological cycle to increasing amounts of greenhouse gases and aerosols. *Climate Dyn.,* **20,** 45–68.

Feichter, J., E. Kjellström, H. Rodhe, F. Dentener, J. Lelieveld, and G. J. Roelofs, 1996: Simulation of the tropospheric sulfur cycle in a global climate model. *Atmos. Environ.,* **30,** 1693–1707.

——, U. Lohmann, and I. Schult, 1997: The atmospheric sulfur cycle and its impact on the shortwave radiation. *Climate Dyn.,* **13,** 235–246.

Ginoux, P., M. Chin, I. Tegen, J. M. Prospero, B. Holben, O. Dubovik, and S. J. Lin, 2001: Sources and distributions of dust aerosols simulated with the GOCART model. *J. Geophys. Res.,* **106,** 20 255–20 273.

Giorgetta, M., and M. Wild, 1995: The water vapour continuum and its representation in ECHAM4. MPI Rep. 162, Max Planck Institute for Meteorology, Hamburg, Germany, 38 pp.

Grassl, H., 1979: Possible changes of planetary albedo due to aerosol particles. *Man's Impact on Climate,* W. Bach, J. Pankrath, and W. Kellogg, Eds., Elsevier, 229–241.

Guenther, A., and Coauthors, 1995: A global-model of natural volatile organic-compound emissions. *J. Geophys. Res.,* **100** (D5), 8873–8892.

Hansen, J., M. Sato, and R. Ruedy, 1997: Radiative forcing and climate response. *J. Geophys. Res.,* **102,** 6831–6864.

Haywood, J. M., R. J. Stouffer, R. T. Wetherald, S. Manabe, and V. Ramaswamy, 1997: Transient response of a coupled model to estimated changes in greenhouse gas and sulfate concentrations. *Geophys. Res. Lett.,* **24,** 1335–1338.

Hess, M., P. Koepke, and I. Schult, 1998: Optical properties of aerosols and clouds: The software package OPAC. *Bull. Amer. Meteor. Soc.,* **79,** 831–844.

Hobbs, P. V., 1999: An overview of the University of Washington airborne measurements and results from the Tropospheric Aerosol Radiative Forcing Observational Experiment (TARFOX). *J. Geophys. Res.,* **104,** 2233–2238.

Jacobson, M. Z., 2001: Strong radiative heating due to the mixing state of black carbon in atmospheric aerosols. *Nature,* **409,** 695–697.

Kettle, A. J., and Coauthors, 1999: A global database of sea surface dimethylsulfide (DMS) measurements and a procedure to predict sea surface DMS as a function of latitude, longitude, and month. *Global Biogeochem. Cycle,* **13,** 399–444.

Kiehl, J. T., and B. P. Briegleb, 1993: The relative roles of sulfate aerosols and greenhouse gases in climate forcing. *Science,* **260,** 311–314.

Kinne, S., and Coauthors, 2003: Monthly averages of aerosol properties: A global comparison among models, satellite date, and AERONET ground data. *J. Geophys. Res.,* **108,** 4634, doi:10.1029/2001JD001253.

Langner, J., and H. Rodhe, 1991: A global three-dimensional model of the tropospheric sulfur cycle. *J. Atmos. Chem.,* **13,** 225–263.

Levkov, L., B. Rockel, H. Kapitza, and E. Raschke, 1992: 3D mesoscale numerical studies of cirrus and stratus clouds by their time and space evolution. *Beitr. Phys. Atmos.,* **65,** 35–58.

Liousse, C., J. E. Penner, C. Chuang, J. J. Walton, H. Eddleman, and H. Cachier, 1996: A global three-dimensional model study of carbonaceous aerosols. *J. Geophys. Res.,* **101** (D14), 19 411–19 432.

Liss, P., and L. Merlivat, 1986: Air–sea gas exchange rates: Introduction and synthesis. *The Role of Air–Sea Exchange in Geochemical Cycling,* P. Buat-Menard, Ed., D. Reidel, 113–128.

Lohmann, U., 2002: Possible aerosol effects on ice clouds via contact nucleation. *J. Atmos. Sci.,* **59,** 647–656.

——, and E. Roeckner, 1996: Design and performance of a new cloud microphysics scheme developed for the ECHAM general circulation model. *Climate Dyn.,* **12,** 12 557–12 572.

——, and ——, 2001: Can the direct and semi-direct aerosol effect compete with the indirect effect on a global scale? *Geophys. Res. Lett.,* **28,** 159–162.

——, and G. Lesins, 2002: Stronger constraints on the anthropogenic indirect aerosol effect. *Science,* **298,** 1012–1015.

——, J. Feichter, C. C. Chuang, and J. E. Penner, 1999: Predicting the number of cloud droplets in the ECHAM GCM. *J. Geophys. Res.,* **104,** 9169–9198.

——, ——, J. E. Penner, and R. Leaitch, 2000: Indirect effect of

sulfate and carbonaceous aerosols: A mechanistic treatment. *J. Geophys. Res.*, **105** (D10), 12 193–12 206.

——, and Coauthors, 2001: Vertical distributions of sulfur species simulated by large scale atmospheric models in COSAM: Comparison with observations. *Tellus*, **53B,** 646–672.

Mahowald, N. M., K. Kohfeld, M. Hansson, Y. Balkanski, S. Harrison, C. Prentice, M. Schulz, and H. Rodhe, 1999: Dust sources and deposition during the last glacial maximum and current climate: A comparison of model results with paleodata from ice cores and marine sediments. *J. Geophys. Res.*, **104,** 15 895–15 916.

Mitchell, J. F. B., 1987: Simulation of climate change due to increased atmospheric carbon dioxide. *Meteor. Mag.*, **116,** 361–376.

Monahan, E. C., D. E. Spiel, and K. L. Davidson, 1986: A model of marine aerosol generation via whitecaps and wave disruption. *Oceanic Whitecaps*, E. C. Monahan and G. McNiocaill, Eds., D. Reidel, 167–174.

Morcrette, J. J., 1991: Radiation and cloud radiative properties in the European Center for Medium Range Weather Forecasts forecasting system. *J. Geophys. Res.*, **96** (D5), 9121–9132.

Penner, J. E., and Coauthors, 2002: A comparison of model- and satellite-derived aerosol optical depth and reflectivity. *J. Atmos. Sci.*, **59,** 441–460.

Ramanathan, V., P. J. Crutzen, J. T. Kiehl, and D. Rosenfeld, 2001: Aerosols, climate and the hydrological cycle. *Science*, **294,** 2119–2124.

——, and Coauthors, 2002: The Indian Ocean Experiment and the Asian brown cloud. *Curr. Sci. India*, **83,** 947–955.

Rasch, P. J., and M. G. Lawrence, 1998: Recent developments in transport methods at NCAR. *Proceedings of the MPI Workshop on Conservative Transport Methods*, B. Machenhauer, Ed., Max Planck Institute for Meteorology Rep. 265, Hamburg, Germany, 65–75.

——, M. Barth, J. T. Kiehl, C. M. Benkovitz, and S. E. Schwartz, 2000a: Description of the global sulfur cycle and its controlling processes in the NCAR CCM3. *J. Geophys. Res.*, **105,** 1367–1385.

——, and Coauthors, 2000b: A comparison of scavenging and deposition processes in global models: Results from the WCRP Cambridge Workshop of 1995. *Tellus*, **52B,** 1025–1056.

Rasool, S. I., and S. H. Schneider, 1971: Atmospheric carbon dioxide and aerosols: Effects of large increases on global climate. *Science*, **173,** 138–141.

Rockel, B., E. Raschke, and B. Weyres, 1991: A parameterization of broad band radiative transfer properties of water, ice and mixed clouds. *Beitr. Phys. Atmos.*, **64,** 1–12.

Roeckner, E., T. Siebert, and J. Feichter, 1995: Climatic response to anthropogenic sulfate forcing simulated with a general circulation model. *Aerosol Forcing of Climate*, R. J. Charlson and J. Heintzenberg, Eds., John Wiley and Sons, 349–362.

——, and Coauthors, 1996: The atmospheric general circulation model ECHAM-4: Model description and simulation of present-day climate, MPI Rep. 218, Max Planck Institute for Meteorology, Hamburg, Germany, 90 pp.

——, L. Bengtsson, J. Feichter, J. Lelieveld, and H. Rodhe, 1999: Transient climate change simulations with a coupled atmosphere–ocean GCM including the tropospheric sulfur cycle. *J. Climate*, **12,** 3004–3032.

Roelofs, G.-J., J. Lelieveld, and J. Feichter, 1998: Model simulations of the changing distribution of ozone and its radiative forcing of climate: Past present and future. MPI Rep. 283, Max Planck Institute for Meteorology, Hamburg, Germany, 24 pp.

——, and Coauthors, 2001: Analysis of regional budgets of sulfur species modelled for the COSAM exercise. *Tellus*, **53B,** 673–679.

Sundqvist, H., E. Berge, and J. E. Kristjansson, 1989: Condensation and cloud parameterization studies with a mesoscale numerical weather prediction model. *Mon. Wea. Rev.*, **117,** 1641–1657.

Tiedtke, M., 1989: A comprehensive mass flux scheme for cumulus parameterization in large-scale models. *Mon. Wea. Rev.*, **117,** 1779–1800.

Timmermann, A., J. Oberhuber, A. Bacher, M. Esch, M. Latif, and E. Roeckner, 1999: Increased El Niño frequency in a climate model forced by future greenhouse warming. *Nature*, **398,** 694–697.

Tselioudis, G., A. D. DelGenio, W. Kovari, and M. S. Yao, 1998: Temperature dependence of low cloud optical thickness in the GISS GCM: Contributing mechanisms and climate implications. *J. Climate*, **11,** 3268–3281.

Williams, K. D., A. Jones, D. L. Roberts, C. A. Senior, and M. J. Woodage, 2001: The response of the climate system to the indirect effects of anthropogenic sulfate aerosol. *Climate Dyn.*, **17,** 845–856.